

# Simulation of motion and radiative decay of Rydberg hydrogen atoms in electric and magnetic fields

M A Henry and F Robicheaux

Department of Physics, Auburn University, AL 36849-5311, USA

E-mail: [robicfj@auburn.edu](mailto:robicfj@auburn.edu)

Received 28 March 2011, in final form 2 June 2011

Published 29 June 2011

Online at [stacks.iop.org/JPhysB/44/145003](http://stacks.iop.org/JPhysB/44/145003)

## Abstract

We have simulated the motion of a Rydberg hydrogen atom in electric and magnetic fields that have a strong position dependence. The orientation and strengths of the fields depend strongly on the spatial position of the atom. The angle between the fields could take on any value. We use the quantum energy levels for a Rydberg state in electric and magnetic fields to derive a spatially dependent potential energy for the centre-of-mass motion of the atom. We compute the radiative decay rate into states with low principal quantum numbers. After the decay, the atom could be trapped using the magnetic moment of the electron. We present results for a specific trap geometry which could be experimentally realized.

## 1. Introduction

There have been several recent studies of the motion of a highly excited atom or molecule under the influence of spatially dependent external fields. One avenue of exploration has focused on the motion in spatially varying electric fields with no magnetic field present. Reference [1] was an early proposal to use the Stark acceleration of Rydberg atoms in an inhomogeneous electric field to decelerate neutral atoms. There have been several recent studies based on this idea. For example, reference [2] was an experimental demonstration of the deflection of krypton Rydberg atoms and reference [3] was an experimental demonstration that molecular hydrogen in Rydberg states could be deflected and decelerated in inhomogeneous electric fields. An extreme example of atomic control of Rydberg atoms in inhomogeneous electric fields was the two-dimensional [4] and three-dimensional [5] trapping of hydrogen atoms. Recently, the deceleration and trapping of Rydberg molecules has also been demonstrated in [6].

Another avenue of exploration has focused on the motion in spatially varying magnetic fields with no electric field present. The experimental push to study the spectroscopy of the antimatter version of the hydrogen atom has reached the milestone of trapping anti-hydrogen in the ground state [7]. The anti-hydrogen is formed when an anti-proton is inside a positron plasma and three-body recombination (an anti-proton and two positrons) leads to a positron weakly bound

in a Rydberg state to the anti-proton. The recombination occurs in magnetic fields of approximately 1 T. Spatially dependent magnetic fields are used to trap the anti-hydrogen in all three dimensions. Thus, it is important for understanding the details of anti-matter experiments to comprehend the centre-of-mass motion and decay of Rydberg atoms moving through inhomogeneous and strong magnetic fields. Before the trapping of anti-hydrogen, the authors of [8] demonstrated the magnetic trapping of cold Rydberg atoms; the atoms were laser cooled and then excited, by photon absorption, to high Rydberg states. Motivated by the prospect of trapping anti-hydrogen, two independent simulations [9, 10] showed that a trapped anti-hydrogen Rydberg atom moving through the inhomogeneous magnetic field would have its centre-of-mass motion cooled during the radiative cascade to the ground state. There have also been theoretical studies of Rydberg atom motion for the situation where the atomic centre-of-mass motion needs to be quantized (for example, see [11]), but these studies require extremely low kinetic energy, well outside the range of parameters of interest here.

One of the main features of anti-hydrogen experiments is that there are both electric and magnetic fields present, with both fields being inhomogeneous, and with the angle between the fields depending on the position in the trap. To our knowledge, how this complication affects the motion of Rydberg atoms has not been studied theoretically although

it appears that experiments are underway to quantitatively address this issue [12].

Since the inhomogeneous electric field case and the inhomogeneous magnetic field case have been studied, it might not be clear that adding both fields together leads to a situation that should be studied theoretically. Motivated by the prospect of detailed experiments [12], we have investigated this system using physically relevant parameters. We have found the case of similar strength electric and magnetic fields with an arbitrary angle between the fields to be extraordinarily challenging when the energy shifts of the states are comparable to or larger than the Rydberg energy spacing. Consequently, we will focus on the situation where the fields give a generalized Stark–Zeeman mixing of states within a degenerate manifold. This restricted case can be solved analytically using degenerate perturbation theory. Because the energies and coefficients of mixing are known analytically, we can efficiently solve for the force on the centre-of-mass motion of the atom and for the decay rate at each position in the trap. But even with the simplification of degenerate perturbation theory, the radiative decay is complicated and we are forced to use further approximations to obtain the properties of the atoms that have decayed to the ground state.

Before getting into the details of the calculation, we can give an estimate of what is meant by similar strength electric and magnetic fields. For this we can compare the maximum energy shift in a pure electric field,  $\simeq n(n-1)3ea_0E/2$ , to that in a pure magnetic field,  $(n-1)\mu_B B$ , where  $e$  is the proton charge,  $a_0$  is the Bohr radius, and  $\mu_B$  is the Bohr magneton. For  $n = 30$  and  $E = 10 \text{ V cm}^{-1}$ , the comparable magnetic field is  $\sim 0.04 \text{ T}$ . For this strength of the electric field and this  $n$ , the maximum energy shift of the Stark effect is  $1.1 \times 10^{-23} \text{ J}$  compared to half of the Rydberg spacing of  $8.1 \times 10^{-22} \text{ J}$ ; thus, the fields could be  $\sim 7\times$  larger without having to consider the level crossing between  $n$ -manifolds. Note that as the principal quantum number increases, the effect of the electric field becomes more dominant.

The next section gives the quantum theory for obtaining the eigenstates and eigenenergies when degenerate perturbation theory is appropriate. The following section gives the description of the classical aspects of the calculation. The final two sections give the results of our simulations and some of the conclusions we have drawn from them.

## 2. Degenerate perturbation theory: non-parallel $E$ and $B$ fields

It is perhaps not as well known as it should be that the eigenstates and eigenenergies within an  $n$ -manifold can be found analytically for arbitrary orientation of the electric and magnetic fields. In this section, we present a short derivation for the sake of completeness. Unless otherwise explicitly stated, we will use atomic units in this section of the paper.

As the basic starting point, we need the commutator relations for the angular momentum and the scaled Runge–Lenz vector. These relations can be found in many graduate textbooks (e.g. [13], chapter 12, section 5, on the Coulomb

potential) with the original derivation by Pauli [14, 15]. The angular momentum operator is given by

$$\vec{L} = \vec{r} \times \vec{p} \quad (1)$$

and the normalized Runge–Lenz vector is given by

$$\vec{a} = n[(\vec{p} \times \vec{L} - \vec{L} \times \vec{p})/2 - \hat{r}] \quad (2)$$

where  $\hat{r} = \vec{r}/r$  is the unit vector in the  $r$ -direction. These vectors have the commutation relations

$$\begin{aligned} [L_i, L_j] &= i\varepsilon_{ijk}L_k \\ [a_i, L_j] &= i\varepsilon_{ijk}a_k \\ [a_i, a_j] &= i\varepsilon_{ijk}L_k, \end{aligned} \quad (3)$$

where  $\varepsilon_{ijk}$  is 1 for  $ijk = (123), (312), (231)$ , is  $-1$  for  $(321), (132), (213)$  and is 0 for the other 21 possible combinations of the indices.

Using these commutation relations, one can show that two commuting angular momenta can be constructed:

$$\vec{J}_1 = \frac{1}{2}(\vec{L} + \vec{a}), \quad \vec{J}_2 = \frac{1}{2}(\vec{L} - \vec{a}), \quad (4)$$

that have the commutation properties

$$\begin{aligned} [J_{1i}, J_{1j}] &= i\varepsilon_{ijk}J_{1k} \\ [J_{2i}, J_{2j}] &= i\varepsilon_{ijk}J_{2k} \\ [J_{1i}, J_{2j}] &= 0 \end{aligned} \quad (5)$$

and that both vectors have squared magnitude equal to  $j(j+1)$  with  $j = (n-1)/2$ . The eigenstates of  $\vec{J}_1^2$  and  $J_{1z}$  can be written as  $|j_1 m_1\rangle$ . Any eigenstate within the  $n$ -manifold can be written as a superposition of all possible products  $|j_1 m_1\rangle |j_2 m_2\rangle$ . As with all angular momenta, there are  $2j+1$  eigenstates for each of these angular momenta. This means there are  $(2j+1) \times (2j+1) = n \times n = n^2$  states altogether.

Within an  $n$ -manifold, the  $\vec{r}$  operator is proportional to the scaled Runge–Lenz vector

$$\vec{r} = \frac{3}{2}n\vec{a} = \frac{3}{2}n(\vec{J}_1 - \vec{J}_2) \quad (6)$$

which will allow us to express the Hamiltonian in terms of the angular momenta.

*Electric field only.* If only an electric field is present, then the  $z$ -direction can be taken to be in the direction of the electric field. For this case, the Hamiltonian,  $H = Ez$ , can be written as

$$H = \frac{3}{2}n(J_{1z} - J_{2z})E \quad (7)$$

which immediately gives the eigenstates as the product of the eigenstates of  $J_{1z}$  and  $J_{2z}$ :  $|j_1 m_1\rangle |j_2 m_2\rangle$  with eigenvalues  $\mathcal{E}_{m_1 m_2} = 3n(m_1 - m_2)E/2$ ; the range of  $m_1$  and  $m_2$  is between  $-(n-1)/2$  and  $(n-1)/2$ . The most extreme blue Stark state is  $m_1 = (n-1)/2$  and  $m_2 = -m_1$ . Because the orbital angular momentum is the sum of  $\vec{J}_1$  and  $\vec{J}_2$ , the connection between the Stark eigenstates and the eigenstates of the orbital angular momentum,  $\ell m$ , is simply the usual vector coupling coefficients:  $\langle \ell m | j_1 m_1 j_2 m_2 \rangle$ . The properties of the vector coupling coefficients means that the usual  $m$  quantum number is the sum  $m = m_1 + m_2$ .

### 2.1. Electric and magnetic fields

The Hamiltonian when both electric and magnetic fields are present is given by

$$H = \vec{E} \cdot \vec{r} + \frac{1}{2} \vec{B} \cdot \vec{L}, \quad (8)$$

where the atomic unit of the magnetic field is  $2.35 \times 10^5$  T. Using the relations above, the Hamiltonian can be transformed into

$$H = \left( \frac{3n}{2} \vec{E} + \frac{1}{2} \vec{B} \right) \cdot \vec{J}_1 - \left( \frac{3n}{2} \vec{E} - \frac{1}{2} \vec{B} \right) \cdot \vec{J}_2 \quad (9)$$

from which we can find the eigenenergies and eigenstates using standard angular momentum manipulations.

**2.1.1. Eigenenergies.** The Hamiltonian in equation (9) is the sum of the operator with only  $\vec{J}_1$  and an operator with only  $\vec{J}_2$ . The eigenvalues of any operator with the form

$$H = \vec{\omega} \cdot \vec{J} \quad (10)$$

can be found by defining  $\vec{\omega}$  to be in the  $z$ -direction. This gives values  $|\vec{\omega}\rangle m$  where  $m$  takes the  $2j + 1$  values from  $-j$  to  $j$  in integer steps. Thus, the eigenvalues corresponding to equation (9) are

$$\mathcal{E}_{m_1 m_2} = \left| \frac{3n}{2} \vec{E} + \frac{1}{2} \vec{B} \right| m_1 - \left| \frac{3n}{2} \vec{E} - \frac{1}{2} \vec{B} \right| m_2 \quad (11)$$

with  $m_1$  taking the  $n$  values from  $-(n-1)/2$  to  $(n-1)/2$  in integer steps and  $m_2$  independently taking the  $n$  values from  $-(n-1)/2$  to  $(n-1)/2$  in integer steps. In SI units, the eigenenergies are

$$\mathcal{E}_{m_1 m_2} = \left| \frac{3nea_0}{2} \vec{E} + \mu_B \vec{B} \right| m_1 - \left| \frac{3nea_0}{2} \vec{E} - \mu_B \vec{B} \right| m_2, \quad (12)$$

where  $e$  is the charge of a proton,  $a_0$  is the Bohr radius, and  $\mu_B$  is the Bohr magneton.

From the expression for the eigenenergies in equation (12), one can obtain the energies for the case  $\vec{E} = 0$  or  $\vec{B} = 0$  and show that they reduce to the usual result. There is a single state that has the largest positive energy shift for the general case of  $\vec{E}$  and  $\vec{B}$ . This state corresponds to  $m_1 = (n-1)/2$  and  $m_2 = -(n-1)/2$  and has the value

$$\mathcal{E}_{\text{ext}} = \left( \left| \frac{3nea_0}{2} \vec{E} + \mu_B \vec{B} \right| + \left| \frac{3nea_0}{2} \vec{E} - \mu_B \vec{B} \right| \right) \frac{n-1}{2} \quad (13)$$

which is always larger than or equal to the shift from the electric field alone or the magnetic field alone. As a final point, for every state  $m_1, m_2$  there is a state with the sign of both  $m_1$  and  $m_2$  flipped which means for every eigenenergy  $\mathcal{E}$ , there is an eigenenergy  $-\mathcal{E}$ .

In atomic units, the most extreme state when the magnetic field is 0 has energy  $\mathcal{E} = 3n(n-1)E/2 \simeq 3n^2E/2$ . We can use this to estimate the electric field where the states of different  $n$ -manifolds cross by setting the shift equal to 1/2 of the Rydberg spacing  $\simeq 1/n^3$ . This gives a limit on  $E$  equal to  $E \leq 1/(3n^5)$ . The most extreme state when the electric field

is 0 has energy  $\mathcal{E} = (n-1)B/2$ . Again comparing this shift to 1/2 of the Rydberg spacing gives  $B \leq 1/n^4$ . If the electric and magnetic field are both present, then the most extreme energy shift occurs when the electric and magnetic fields are perpendicular. The most extreme state will have as its maximum energy shift  $\mathcal{E} = \sqrt{(3nE)^2 + B^2(n-1)}/2$ . Again comparing this to 1/2 the spacing gives  $\sqrt{(3nE)^2 + B^2} \leq 1/n^4$ . If the electric and magnetic fields satisfy this condition, then the perturbative treatment in this paper should be accurate.

**2.1.2. Eigenvectors.** In order to compute the radiative decay from an eigenstate, we need to find the transformation from the  $m_1 m_2$  states to the  $\ell m$  states. The nature of the Hamiltonian allowed us to write down the eigenenergies in a simple form. The eigenvectors are somewhat more complicated but can also be found in terms of standard operations.

Since we only need the eigenvectors to compute the radiative decay rate, we do not need to worry about the overall orientation of the vectors. However, the relative direction of the  $\vec{E}$  and  $\vec{B}$  are crucial. Therefore, we will take the electric field to be in the  $z$ -direction and we will take the part of  $\vec{B}$  that is not parallel to  $\vec{E}$  to be in the  $x$ -direction. Another way of thinking about the orientation of  $\vec{B}$  is that the vector  $\vec{E} \times \vec{B}$  is in the  $y$ -direction. With these definitions, the Hamiltonian of equation (9) is transformed into

$$H = \left[ \left( \frac{3En}{2} + \frac{B_z}{2} \right) J_{1z} + \frac{B_x}{2} J_{1x} \right] - \left[ \left( \frac{3En}{2} - \frac{B_z}{2} \right) J_{2z} - \frac{B_x}{2} J_{2x} \right] \quad (14)$$

with  $B_z = \vec{E} \cdot \vec{B}/|\vec{E}|$  and  $B_x = \sqrt{B^2 - B_z^2}$ . We can simplify this Hamiltonian to

$$H = \mathcal{E}_1 [J_{1z} \cos \theta_1 + J_{1x} \sin \theta_1] - \mathcal{E}_2 [J_{2z} \cos(-\theta_2) + J_{2x} \sin(-\theta_2)] \quad (15)$$

where

$$\mathcal{E}_1 = \frac{1}{2} \sqrt{(3En + B_z)^2 + B_x^2} \quad \tan \theta_1 = \frac{B_x}{3En + B_z} \quad (16)$$

and

$$\mathcal{E}_2 = \frac{1}{2} \sqrt{(3En - B_z)^2 + B_x^2} \quad \tan \theta_2 = \frac{B_x}{3En - B_z} \quad (17)$$

define the energies and angles in equation (15).

With the Hamiltonian in the form of equation (15), we can use the relation

$$J_z \cos \theta + J_x \sin \theta = e^{-i\theta J_y} J_z e^{i\theta J_y} \quad (18)$$

and the fact that  $\vec{J}_1$  commutes with  $\vec{J}_2$  to obtain

$$H = e^{-i\theta_1 J_{1y}} e^{i\theta_2 J_{2y}} (\mathcal{E}_1 J_{1z} - \mathcal{E}_2 J_{2z}) e^{i\theta_1 J_{1y}} e^{-i\theta_2 J_{2y}}. \quad (19)$$

From this form of the Hamiltonian, one can show that the eigenvectors,  $H|\psi\rangle_{m_1 m_2} = \mathcal{E}_{m_1 m_2} |\psi\rangle_{m_1 m_2}$ , must be equal to

$$|\psi\rangle_{m_1 m_2} = e^{-i\theta_1 J_{1y}} e^{i\theta_2 J_{2y}} |j_1 m_1\rangle |j_2 m_2\rangle, \quad (20)$$

where each rotation matrix only acts on the vector for the corresponding angular momentum.

Now that we have the eigenvectors we can project them onto the  $\ell m$  state to obtain the amplitude to be in a particular orbital angular momentum state. The amplitude to be in the state  $n\ell m$  is

$$\langle \ell m | \psi \rangle_{m_1 m_2} = \sum_{\bar{m}_1 \bar{m}_2} \langle \ell m | j_1 \bar{m}_1 j_2 \bar{m}_2 \rangle \langle j_1 \bar{m}_1 | e^{-i\theta_1 J_{1y}} | j_1 m_1 \rangle \times \langle j_2 \bar{m}_2 | e^{i\theta_2 J_{2y}} | j_2 m_2 \rangle, \quad (21)$$

where the first term after the summation symbol is the usual vector coupling coefficient and the last two terms are the unitary rotation matrices  $d_{\bar{m}m}^{(j)}(\theta)$  [16].

There was one technical difficulty we had in computing the amplitude to be in the state  $n\ell m$ . The large magnitude of the  $J_y$  and the large possible size of the angle led to difficulties in computing the rotation matrices. Since  $n\theta$  could be as large as  $\sim 100$ , computing the rotation matrices by a power series expansion leads to cases where the roundoff error was larger than the result. We solved this problem by computing the rotation matrix for the angle  $\theta/2^k$  with  $k$  an integer large enough that  $n\theta/2^k < 0.1$ ; because the angle was small, a power series expansion was efficient and stable. We multiplied the resulting matrix on itself to get the rotation matrix at the angle  $\theta/2^{k-1}$ . We repeated this process until we obtained the rotation matrix for the angle  $\theta$ . We found this method to be both efficient and stable for any angle we needed.

## 2.2. Adiabatic approximation

In computing the motion of the atom, we assumed that  $m_1$  and  $m_2$  are conserved until a photon is emitted. This is an approximation that assumes that the state adiabatically follows the appropriately combined directions of the electric and magnetic fields. This approximation does *not* fail when the eigenenergy  $\mathcal{E}_{m_1 m_2}$  goes to 0 because the Hamiltonian is the sum of two commuting terms:  $H = \vec{\omega}_1 \cdot \vec{J}_1 - \vec{\omega}_2 \cdot \vec{J}_2$ . This approximation fails when the atom goes through a region where either of the two vectors defined by

$$\hbar \vec{\omega}_{1,2} = \frac{3ne a_0}{2} \vec{E} \pm \mu_B \vec{B} \quad (22)$$

goes to 0; this equation is given in SI units for ease of calculation. For the adiabatic approximation to fail, the direction of  $\vec{\omega}_1$  must be changing faster than the magnitude  $|\vec{\omega}_1|$  or the direction of  $\vec{\omega}_2$  must be changing faster than the magnitude  $|\vec{\omega}_2|$ . This can occur in a small volume around the points where one of the vectors is exactly 0.

These regions are very small. As an estimate we will take the rate of change of the direction to be a representative speed (100 m s<sup>-1</sup> corresponds to  $\sim 0.6$  K) divided by a representative size for the trap (1 mm) to obtain  $\sim 10^5$  rad s<sup>-1</sup>. This would correspond to a change in the electric field of  $\hbar 10^5$  rad s<sup>-1</sup> / (3ne a<sub>0</sub>/2)  $\sim 0.3$  mV cm<sup>-1</sup> for  $n = 30$  or a change in the magnetic field of  $\hbar 10^5$  rad s<sup>-1</sup> /  $\mu_B \sim 10^{-6}$  T. Our magnetic field has a variation of  $\sim 100$  T m<sup>-1</sup> which gives a corresponding distance of  $\sim 10^{-6}$  T / (100 T m<sup>-1</sup>) =  $10^{-8}$  m. The electric field has a variation of order  $\sim 30$  V cm<sup>-1</sup> mm<sup>-1</sup> which gives a corresponding distance of  $\sim 0.3$  mV cm<sup>-1</sup> / (30 V cm<sup>-1</sup> mm<sup>-1</sup>) =  $10^{-8}$  m. To be

safe, we considered the motion to be adiabatic if the atoms did not pass within  $10^{-7}$  m of the non-adiabatic points.

For the electric and magnetic fields given below, these vectors only go to zero at a few points near the edge of the trapping region. We found that these regions did not affect any of the trajectories in section 4. Thus, the adiabatic approximation works well for the fields below. It should be noted that a different choice of fields could lead to zeros in the middle of the regions that the atoms traverse multiple times.

## 2.3. Radiative decay rates

For the correct quantum calculation of decay rates, we need to solve for the dipole matrix elements for a state  $nm_1 m_2$  to all states with principal quantum number less than  $n$ . To correctly simulate the atom motion after a radiative transition, we need to know all of the final state quantum numbers. Because of the large multiplicity of states, this is not feasible for the high quantum numbers we studied. The difficulty is that every time step will give a new  $\theta_1$  and  $\theta_2$  in the eigenfunction which leads to a position-dependent decay rate and a position-dependent branching ratio to final  $n'm'_1 m'_2$ . To understand the radiative cascade process, we solved for the transitions at different positions within the trap for several different initial states. We found that the most rapid decay path is usually a single photon to  $n \leq 10$  with a subsequent fast decay to the ground state. When there is no electric field, the atom goes to a circular state so that the only possible decay is the sequence  $n \rightarrow n-1 \rightarrow n-2 \dots$ . Because there is usually an angle between the electric and magnetic field, the  $\ell m$  mixing is such that there are often low  $\ell$  components in the wavefunction which will allow decay to smallish  $ns$  in one step.

The decay from a specific  $nm_1 m_2$  state to a state with  $n'm'_1 m'_2$  is difficult because both the initial and final state coefficients are needed to compute the three-dipole matrix elements:  $\langle nm_1 m_2 | x | n'm'_1 m'_2 \rangle$  and similar for  $y$  and  $z$ . There are approximately  $n^3/3$  states with  $n' < n$  giving approximately  $n^3$  matrix elements that need to be calculated. (If black body radiation is an important issue, the matrix elements to states with  $n' > n$  also need to be calculated.)

It is much easier to obtain the decay rate from a state  $nm_1 m_2$  into all of the states in an  $n$ -manifold. The rate to decay from the state  $nm_1 m_2$  into all states of the  $n'$  manifold only depends on the sum of the angles  $\theta_1, \theta_2$  and is given by

$$\Gamma_{nm_1 m_2 \rightarrow n'} = \sum_{\ell m} \Gamma_{n\ell \rightarrow n'} |\langle \ell m | \psi \rangle_{m_1 m_2}|^2, \quad (23)$$

where  $\langle \ell m | \psi \rangle_{m_1 m_2}$  is defined in equation (21),  $\Gamma_{n\ell \rightarrow n'}$  is the decay rate in the 0 field from a state with quantum numbers  $n\ell$  into all states of the  $n'$  manifold.

Figure 1 shows the total radiative decay rate for the  $n = 30$ ,  $m_1 = 29/2$  and  $m_2 = -29/2$  as a function of  $\theta = \theta_1 + \theta_2$ . The different lines show decay into all final states with  $n \leq 10, 15, 20, 25$  and 29. There are a couple of important features of this graph to be noted. The first is that the peak decay rate is when  $\theta$  is small; the reason for this is that the case of  $\theta \sim 0$  is the case of the blue Stark state with  $m = 0$  which has a large composition of low angular momenta which radiate quickly. Another important feature is that most

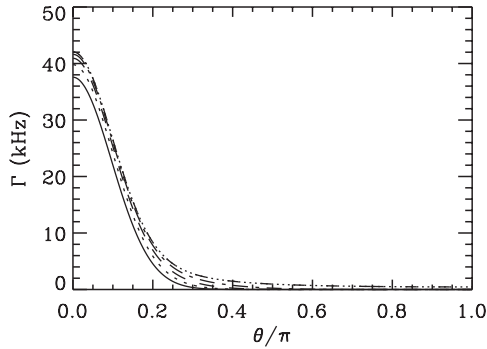


**Figure 1.** The total radiative decay rate for  $n = 30$ ,  $m_1 = 29/2$ , and  $m_2 = -29/2$  as a function of  $\theta = \theta_1 + \theta_2$ . The different lines show decay into all final states with  $n \leq 10$  (solid line), 15 (dotted line), 20 (dashed line), 25 (dash-dot line) and 29 (dash-dot-dot line).

of the decay goes directly into states with  $n \leq 10$ ; states with  $n \leq 10$  account for 90% of the decay rate at  $\theta = 0$ . Finally, at large angles, the decay rate is small and it is almost all into states with  $n > 25$ . This is because when  $\theta \sim \pi$  this state is essentially the circular state with  $\ell = n - 1$  and  $m = \ell$ ; this state can only decay by going from  $n \rightarrow n - 1$ . Although decay into high  $n$  is important for  $\theta \sim \pi$ , the rate is only  $\sim 1$ –2% of the peak rate.

Below we will describe how we compute the motion of the hydrogen atom. It is important to realize that the motion of the hydrogen atom means that the decay rate changes with time because the angle  $\theta = \theta_1 + \theta_2$  is changing. While it is possible to compute all of the decay rates from  $nm_1m_2$  into  $n'm'_1m'_2$  from a quantum treatment of the hydrogenic energy levels, the number of times that this calculation will be necessary as the hydrogen moves through the fields precludes accounting for all of the states. We resorted to the approximation of limiting the decay from the initial state into states with  $n \leq 10$  and then assuming that the subsequent decay occurs quickly enough that the hydrogen atom hardly moves during the transition to the ground state. This approximation will underestimate the decay rate by a factor of roughly 10%. This approximation will also cause our centre-of-mass kinetic energy distribution for ground state atoms to be somewhat hotter than that which would result from a full calculation; the reason is that some atoms move during the last parts of the cascade and that motion will provide some centre-of-mass cooling as in [9, 10].

In the calculations below, we will start in several different initial states. Figure 2 shows the decay rate into states with  $n \leq 10$  for five of the most blue-shifted states with  $n = 30$ :  $(m_1, m_2)$  equal to  $(29/2, -29/2)$ ,  $(27/2, -27/2)$ ,  $(25/2, -25/2)$ ,  $(29/2, -27/2)$  and  $(29/2, -25/2)$ . The decay rate for the state  $(29/2, -27/2)$  is the same as that for the state  $(27/2, -29/2)$  and for the state  $(-29/2, 27/2)$ . All of the states radiate most strongly for  $\theta < 1$  but the most extreme state radiates most strongly.

We chose to investigate these states because they are probably of most interest for trapping atoms. These states are the ones that are most strongly trapped by the fields. If the signs of both  $m_1$  and  $m_2$  are flipped, the resulting state has electric and magnetic dipole moments that give a force that

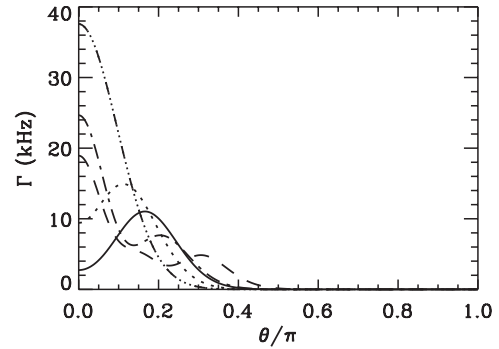


**Figure 2.** The decay rate into states with  $n \leq 10$  for five states with  $n = 30$ :  $(m_1, m_2)$  equal to  $(29/2, -29/2)$  (dash-dot-dot-dot line),  $(27/2, -27/2)$  (dash-dot line),  $(25/2, -25/2)$  (dashed line),  $(29/2, -27/2)$  (dotted line) and  $(29/2, -25/2)$  (solid line).

repels the atom from the trap. Thus, requiring strong trapping leads to an investigation of states with large, positive values for  $m_1 - m_2$ . In the experiments of Rydberg atoms in static electric fields, the atoms are excited from very deeply bound states into the Rydberg states with one or two photons. This method of excitation means that the  $m$  is small which implies that  $|m_1 + m_2|$  is a small integer (less than 3).

For the calculations below, we only include the spontaneous radiative decay rate. The recent results in [17] showed that black body radiation can play an important role if the temperature is high. The authors of [17] saw strong effects at 300 K but weak effects at 125 K. In the anti-matter experiments, the black body radiation will not be an issue if the radiation field is at the temperature of the trap (less than  $\sim 10$  K). The black body transitions are dominant for small changes in  $n$ . Unfortunately, the calculation of dipole matrix elements for states separated by small  $n$  are those which are too time consuming to compute (as explained earlier in this section). Thus, our calculations are limited to low temperature for the black body radiation.

We note that there are several papers that have given compact expressions for radiative decay based on semiclassical approximations. Unfortunately, these results are not useful for us because they are for the total decay rate of states. We need the transition rate from a specific initial state  $nm_1m_2$  to a specific final state  $n'm'_1m'_2$  because all three quantum numbers determine the force that the atom feels after the decay. It is possible that there is a way of obtaining these rates using a semiclassical approximation, but none of the existing methods seem to be applicable to our situation.

### 3. Classical motion

This section describes the parameters that went into computing the motion of the hydrogen atom.

#### 3.1. Electric field

We needed to choose a form for the electric field. The authors of [5] demonstrated three-dimensional trapping of hydrogen Rydberg atoms using only electrostatic fields. In figure 1 of [5], they show two cuts of the electric field. We used this data to fit a simple form for the electrostatic potential. The strategy

**Table 1.** The coefficients of the electrostatic potential used in this calculation.

|       |             |       |             |       |             |
|-------|-------------|-------|-------------|-------|-------------|
| $c_1$ | -1.08553E03 | $c_2$ | -2.07143E07 | $c_3$ | -1.20814E11 |
| $c_4$ | 7.50741E04  | $c_5$ | 2.53946E06  | $c_6$ | -1.13210E09 |
| $c_7$ | -9.25872E08 | $c_8$ | -1.28327E09 | $c_9$ | -8.60316E10 |

was to have an electrostatic potential which was the sum of several terms, each of which satisfies Laplace's equation and approximated the symmetry of their electrodes. We chose

$$\begin{aligned}
 V = & c_1x + c_2[2x^3 - 3x(y^2 + z^2)] + c_3[8x^5 - 40x^3(y^2 + z^2) \\
 & + 15x(y^2 + z^2)^2] + c_4\frac{1}{2}(z^2 - y^2) + c_5zy \\
 & + c_6\frac{1}{2}(z^2 - y^2)[6x^2 - (y^2 + z^2)] \\
 & + c_7[6x^2 - (y^2 + z^2)]yz + c_8(y^4 - 6y^2z^2 + z^4) \\
 & + c_9(yz^3 - y^3z), \tag{24}
 \end{aligned}$$

where the coefficients in SI units are given in table 1. Using these coefficients, we were able to fit the data in their figure 1 when  $|x| < 5$  mm,  $|y| < 2.3$  mm and  $|z| < 3$  mm. Whenever a hydrogen atom went beyond this region, we counted it as leaving the trap.

The electric field was obtained by the usual expression  $\vec{E} = -\vec{\nabla}V$ . Because we have the potential in a smooth polynomial form, the calculation of the electric field was fast enough for the classical calculation of the motion of the atom described below.

### 3.2. Magnetic field

For the magnetic field, we took a simple linear form which would approximate the magnetic field near the 0 in an anti-Helmholtz configuration. In some of the calculations below, we allow the axis of symmetry to change. Taking the unit vector  $\hat{s}$  to be along the axis of symmetry, we defined our magnetic field to be

$$\begin{aligned}
 B_x &= \mathcal{B}\frac{1}{2}[3\hat{s}_x(\hat{s} \cdot \vec{r}) - x] \\
 B_y &= \mathcal{B}\frac{1}{2}[3\hat{s}_y(\hat{s} \cdot \vec{r}) - y] \\
 B_z &= \mathcal{B}\frac{1}{2}[3\hat{s}_z(\hat{s} \cdot \vec{r}) - z], \tag{25}
 \end{aligned}$$

where  $\mathcal{B} = 120$  T m<sup>-1</sup>. As with the electric field, the calculation of the magnetic field was fast enough for our simulations of the atom motion.

### 3.3. Classical motion

We solved for the centre-of-mass motion of the hydrogen atom using the classical equations of motion

$$\frac{d\vec{R}}{dt} = \vec{V} \quad \frac{d\vec{V}}{dt} = \frac{\vec{F}}{M}, \tag{26}$$

where  $\vec{R}$  is the position of the atom in the trap,  $\vec{V}$  is the velocity of the atom,  $\vec{F}$  is the force on the atom and  $M$  is the mass of the atom. The force is obtained by taking the gradient of the potential energy

$$\vec{F} = -\vec{\nabla}\mathcal{E}_{m_1m_2}, \tag{27}$$

where the  $\mathcal{E}_{m_1m_2}$  is from equation (12). The position dependence of the electric and magnetic fields are as described

above. We did not analytically compute the gradient. Instead, we computed the potential energy at points slightly separated in space and computed the central difference, for example, the points  $(X + \delta X, Y, Z)$  and  $(X - \delta X, Y, Z)$  were used to compute the  $x$ -component of the force at the point  $(X, Y, Z)$ . We checked the convergence with respect to the spacing of points by checking that energy was conserved during the motion. We also checked convergence by performing runs with the spacing decreased by a factor of 2; since the central difference has error proportional to the cube of the spacing, obtaining the same trajectory with a decreased spacing shows that the error from the finite difference was negligible.

To somewhat mimic the initial conditions that might be obtained in an experiment, we started our atoms with random positions and velocities. The velocity components were chosen from a thermal distribution with a different temperature in each direction: the  $x$ -component was a temperature of 75 mK, the  $y$ -component was 2 mK and the  $z$ -component was 300 mK. The distribution of positions was chosen from a distribution proportional to  $\exp(-PE/[0.2 \text{ K } k_B])$  with the  $PE$  calculated only using the electric field. We chose this spatial distribution because launching the atoms exactly from the origin would give an unphysically biased distribution of trajectories. We know from experiments that the temperature of the atoms in the trap with only an electric field is approximately 150 mK. These temperatures were chosen to be relevant for recent experiments [5].

We solved the classical equations of motion using an adaptive step-size fourth order Runge-Kutta algorithm [18]. We could check the convergence of the trajectory by changing the accuracy parameter and making sure that the same trajectory resulted from the same initial conditions.

To give an idea of the structure of the trap, figure 3 shows the potential energy of the atom as a contour for two orthogonal cuts through the trap. The potential energy is for the state  $n = 30$ ,  $m_1 = 29/2$  and  $m_2 = -29/2$ . For the magnetic field, we chose  $\hat{s} = \hat{x}$ . The potential energy has a depth of several kelvin from the origin to the edge where we count the atom as having escaped. For this state, there are comparable contributions to the potential from the electric and magnetic field which leads to a greater potential depth and also a change in the shape of the potential.

The radiative decay was included using a statistical procedure. The radiative decay rate was computed in each time step and the probability for decay was computed:  $P = 1 - \exp(-\Gamma_{nm_1m_2}\delta t)$ , where  $\delta t$  was the time step and  $\Gamma_{nm_1m_2}$  is the decay rate into all states with  $n \leq 10$ . A random number with a flat distribution between 0 and 1 is then generated. If the random number is less than  $P$ , then the atom is counted as having decayed. If the random number is greater than  $P$ , then we continue to propagate the classical motion of the atom for another time step.

To give an idea of where the atom preferentially decays as a function of position, figure 4 shows the decay rate as a contour for two orthogonal cuts through the trap shown in figure 3. The decay rate is for the state used in figure 3:  $n = 30$ ,  $m_1 = 29/2$  and  $m_2 = -29/2$ . In the  $xz$ -plane, the emission rate is high only near the centre of the trap because

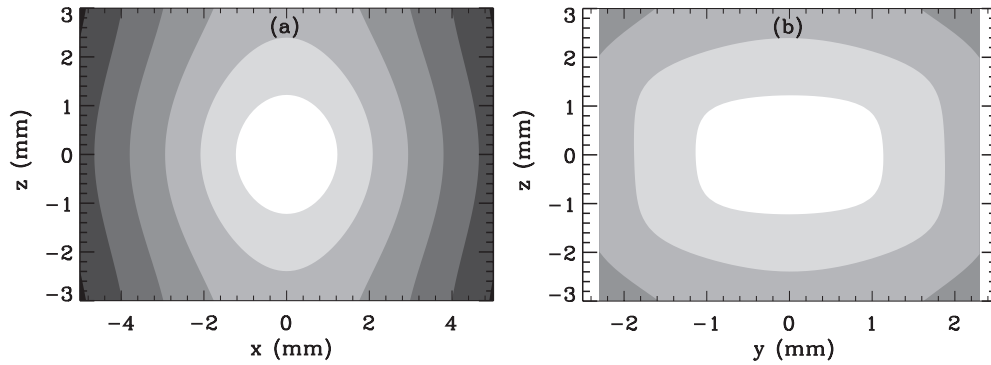


**Figure 3.** The potential energy for the  $(29/2, -29/2)$  for two different cuts through the three-dimensional trap: (a) the  $xz$ -plane and (b) the  $yz$ -plane. The plots are for the range of values of figure 1 of [5]. The contour levels are the same for both graphs and correspond to steps by 2 K. White corresponds to 0–2 K, lightest grey corresponds to 2–4 K, etc.

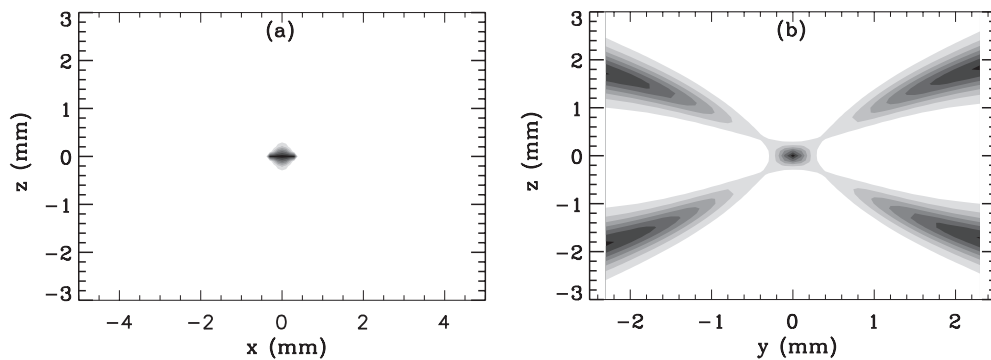


**Figure 4.** The radiative decay rate into states with  $n \leq 10$  for the  $(29/2, -29/2)$  for two different cuts through the three-dimensional trap: (a) the  $xz$ -plane and (b) the  $yz$ -plane. The contour levels are the same for both graphs and corresponds to steps by  $5 \times 10^3 \text{ s}^{-1}$ . White corresponds to  $0\text{--}5 \times 10^3 \text{ s}^{-1}$ , lightest grey corresponds to  $5 \times 10^3\text{--}10 \times 10^3 \text{ s}^{-1}$  . . . , black corresponds to  $35 \times 10^3\text{--}40 \times 10^3 \text{ s}^{-1}$ .

near the centre of the trap the magnetic field is small and the state is like a Stark state. In the  $yz$ -plane, the magnetic field points radially outward. The angles at multiples of  $45^\circ$  give magnetic fields essentially parallel to the electric field. This gives a small value of  $\theta_1 + \theta_2$  which leads to a high decay rate.

## 4. Results

In this section, we present some of the results from our calculations.

### 4.1. Decay rate

Figure 5 shows the number of decays per unit time which is the decreasing function of time because the number of Rydberg atoms is getting smaller with time. The slope in the inset gives an indication of the decay rate of the remaining Rydberg atoms. The plots are on an arbitrary scale on the y-axis but the time integral from  $t = 0$  to  $\infty$  is the same for all curves. In all of the calculations, the magnetic field has been set to have  $\hat{s} = \hat{x}$ . The decay rate is for five different initial quantum states with  $n = 30$ :  $(29/2, -29/2)$  dash-dot-dot-dot line,  $(27/2, -27/2)$  dash-dot line,  $(25/2, -25/2)$  dashed line,  $(29/2, -27/2)$  dotted line and  $(29/2, -25/2)$  solid line. Over the main part of the decay, the different initial states have

similar decay rates compared to the disparity in the rates of figure 2. The state with the fastest decay is the  $(29/2, -29/2)$  state as in figure 2 but it is only a factor of  $\sim 1.5$  faster than the slowest state; the peak decay rate for this state in figure 2 is a factor of  $\sim 4$  larger than the peak of the slowest decay rate. The reason for the smaller spread in actual decay rates will be discussed in the next section. The time to reach  $1/e$  of the initial rate is between approximately 0.2 and 0.4 ms. This is a decay rate that is a factor of 5–10 higher than the rate at large angles shown in figure 1. We think that ignoring the decay through the high  $n$  states will change the quantitative values we obtain but probably will not affect the general conclusions because the actual decay rate seen in figure 5 is much larger than the correction.

On the log-scale shown in the inset, the behaviour of the decay rate at longer times can be seen. For all of the initial states, the decay rate at early time is higher than the decay rate at later times. This is because there are a range of average decay rates depending on the motion of the atom; some atoms spend a larger time in regions of space where the decay rate is smaller and these are more likely to survive to longer times. Another interesting feature is that the  $(29/2, -29/2)$  state starts out with the fastest decay rate, but it becomes somewhat slower than the others at later times although it is difficult to see because of the statistical noise. This seems due to the decay rate in figure 2 which shows that if the atom spends a

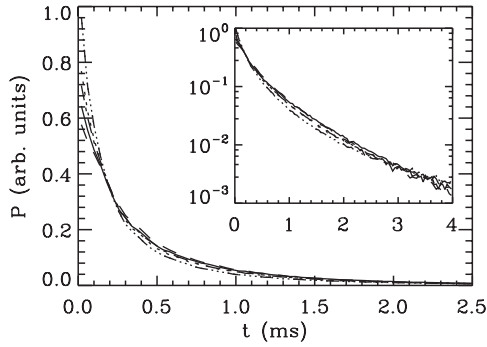


**Figure 5.** The number of decays per unit time for the states of figure 2. The line types are the same as in figure 2.

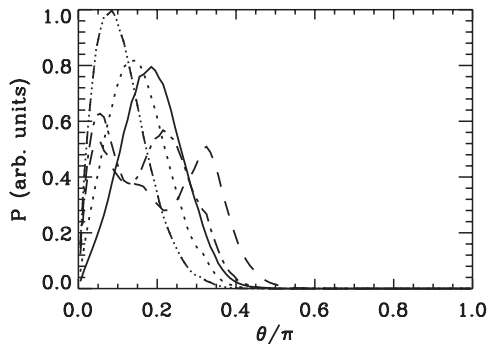


**Figure 6.** The probability,  $P$ , for a radiative decay to occur during a small interval at the angle  $\theta = \theta_1 + \theta_2$ . The states and the line types are the same as in figure 2.

large fraction of the time in regions where  $\theta > 0.2$ , then this is the state with the smallest decay rate.

The results in this and the next three sections depend on the distribution of the initial population. If the population substantially changes, then the results can be different. We also performed calculations with a temperature about  $10\times$  higher than that presented here. For this population, we found that the decay rates were smaller because the atoms spent more time in regions of space where the  $\theta_1 + \theta_2$  was larger. However, we found that two of the general features were the same: (1) the decay rates are more similar than those which might be expected by figure 2 and (2) the  $(29/2, -29/2)$  state starts with the largest decay rate but has the smallest decay rate at later times.

#### 4.2. Distribution of $\theta = \theta_1 + \theta_2$

We stored the relative angle  $\theta = \theta_1 + \theta_2$  when the atom decayed and binned the result. Figure 6 shows the distribution of  $\theta$  when the atom decayed for the five different states used in figure 5. The line types in figure 6 are the same as those of figure 5. This figure should be compared to the decay rate versus  $\theta$  which is plotted in figure 2. Both plots show that the majority of the decays occur for angles less than  $\sim 1.2$  rad; this makes sense in that the decay will mainly occur when the rate is high.

However, although the distributions in figure 6 are related to the plots of figure 2, they differ in a fundamental way. The

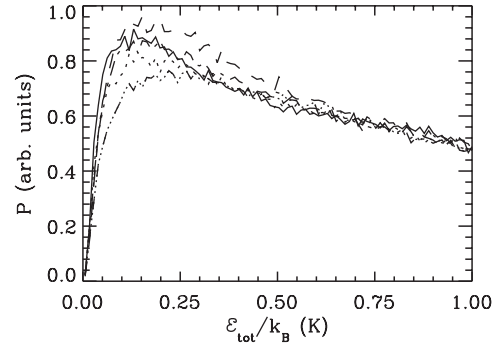


**Figure 7.** The probability,  $P$ , for the atom to be in a small interval at the energy,  $\mathcal{E}_{\text{tot}}$ , after the radiative decay. The states and the line types are the same as in figure 2 and  $k_B$  is Boltzman's constant.

main feature is that the plots in figure 6 go to 0 as  $\theta \rightarrow 0$  whereas the decay rates in figure 2 go to finite values. The reason for the difference is simply due to the relative size of phase space. The region of space where  $\theta$  is in a small range of size  $d\theta$  is proportional to  $\sin\theta d\theta$ . We plotted the decay rate of figure 2 times  $\sin\theta$  and scaled to the size of the data shown in figure 6 and found that there was good reproduction of the binned data out to  $\theta \sim 0.7$  rad, but the agreement is not perfect because the actual time distribution of  $\theta$  is not exactly statistical.

Figure 6 helps to explain why the decay rates in figure 5 are more similar than those that might be expected from figure 2. In figure 6, we see that the peak of the decays versus  $\theta$  occurs at  $\sim 0.1$  rad for the  $(29/2, -29/2)$  state and there are many decays for angles larger than this. By  $\theta \sim 0.1$  rad, the decay rate for the  $(29/2, -29/2)$  has dropped by a factor of  $\sim 2$  and is similar in value to the other states. Also, the atoms do spend time at even larger  $\theta$  where the  $(29/2, -29/2)$  state has the smallest decay rate.

#### 4.3. Energy distribution

In [9, 10], it was found that the centre-of-mass kinetic energy of the atoms cooled during a radiative cascade. Figure 7 shows the energy distribution of the atoms when they reach their ground state with the focus being on the low energy part of the distribution. The states and line types are the same as in figures 5 and 6. The energy is computed as the kinetic energy plus the magnetic potential energy assuming the atom cascaded to the state with the appropriate spin

$$\mathcal{E}_{\text{tot}} = (KE + |\vec{B}| \mu_B) \quad (28)$$

where  $\mu_B$  is the Bohr magneton. The overall normalization of the y-axis is arbitrary but the integral of the distribution from 0 to  $\infty$  is the same for all states.

The states start with the same initial energy distribution but the final distributions depend on which is the initial state of the atom although there are not large differences between these states. The  $(25/2, -25/2)$  and  $(29/2, -25/2)$  states end up with the most low energy atoms after the decay and the  $(29/2, -29/2)$  state has the least number of low energy atoms. Since the Bohr magneton is approximately  $2/3 \text{ K T}^{-1}$ ,



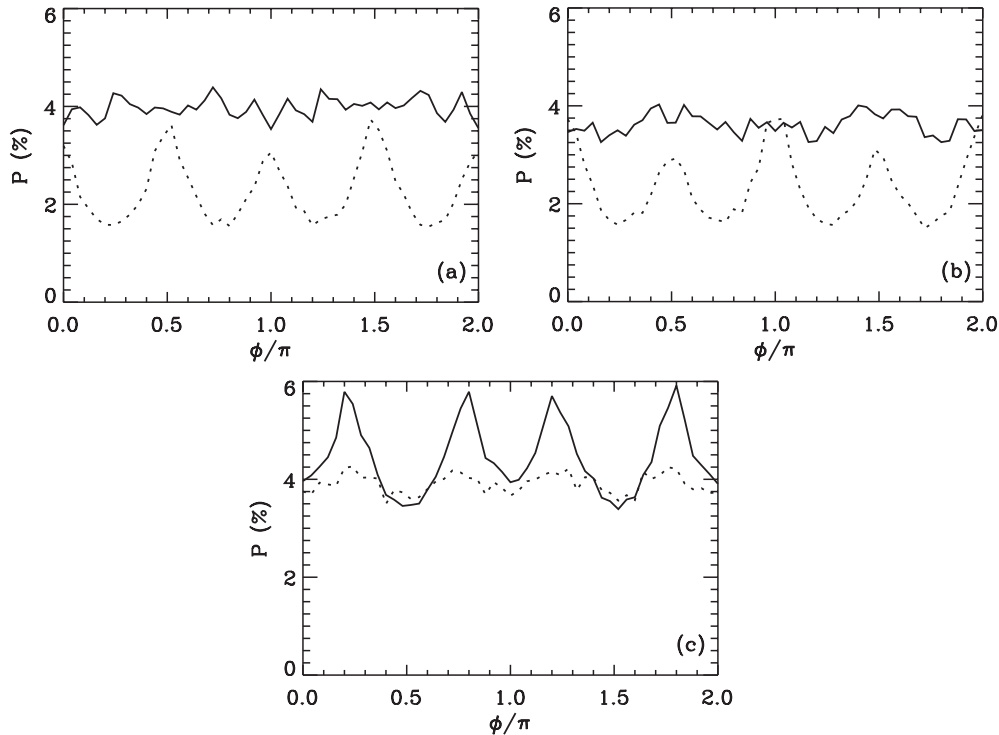


**Figure 8.** The probability,  $P$ , for the atom to have a total energy less than  $0.1 \text{ K} \times k_B$  after the radiative decay (solid line) as a function of the orientation of the magnetic field; atoms in a magnetic well with a depth of  $\sim 0.15 \text{ T}$  would trap these atoms. The dotted line is the probability times a factor of 2 for the atom to *start* with an energy less than  $0.1 \text{ K} \times k_B$ . (a) The orientation of the magnetic field is defined by  $\hat{s} = (\cos \phi, \sin \phi, 0)$ . (b) The orientation of the magnetic field is defined by  $\hat{s} = (\sin \phi, 0, \cos \phi)$ . (c) The orientation of the magnetic field is defined by  $\hat{s} = (0, \cos \phi, \sin \phi)$ .

atoms with an energy of  $1 \text{ K}$  will need to be in a magnetic well depth of  $1.5 \text{ T}$  to remain bound.

There is cooling that occurs because of the decay, but the effect is not as big as in [9]. This result was a surprise to us because the change in quantum number is larger in the current calculation. We think there are two reasons for the smaller effect in our calculation. First, the spontaneous decay rate in [9, 10] only weakly depended on the position of the atom in the trap; thus, from simple phase space arguments, the atom is most likely to decay where the speed is small in [9, 10]. In the present calculations, the decay rate is enhanced at the centre of the trap where the speed is highest which means the atom is more likely to emit a photon when it has substantial kinetic energy. Second, the potential energy function after the decay is  $|\vec{B}|\mu_B$  which is linear in the distance from the origin but before the decay it is given by equation (12) which is quadratic in the distance from the origin. In [9, 10], the potential energy before and after the photon emission was proportional to  $|\vec{B}|$ . This can have an effect because a lower final energy is achieved if the potential energy before the photon emission is approximately proportional to the potential energy after the emission. To see how this works, suppose the atom emits the photon when its speed is 0. If the potential energy before and after the emission are proportional to each other, the final energy is the initial energy times the ratio of final magnetic moment to initial magnetic moment. In the present calculation, the ratio of final to initial potential energy will depend strongly on position; because the final potential energy is proportional to

the distance from the centre of the trap, the ratio is not nearly as small as in [9, 10].

#### 4.4. Low energy versus magnetic field orientation

We investigated whether the orientation of the magnetic field would affect the fraction of the atoms that finished with a small energy after the decay. We arbitrarily chose the small energy to be  $0.1 \text{ K} \times k_B$ . The results are shown as solid lines in figure 8 for rotation of the magnetic field orientation about three different axes: (a) shows rotation in the  $xy$ -plane, (b) shows rotation in the  $zx$ -plane and (c) shows rotation in the  $yz$ -plane. Half of the range plotted is redundant because the same magnetic field results when  $\hat{s} \rightarrow -\hat{s}$ .

It is clear from the figure that the orientation of the magnetic field with respect to the electrostatic trap can play a large role in the fraction of atoms that have low energy after the decay. This graph shows that the fraction of atoms trapped in a shallow well could depend in a crucial way on the orientation of the magnetic field. The ratio of  $\max(P)/\min(P) \sim 2$  which is probably large enough to worry about. We did not test for arbitrary orientations of the magnetic field so there could be some directions where the number of low energy atoms is very strongly enhanced or suppressed.

One possible source of this change could be that the initial potential energy of the atom is changing with the orientation. The dotted line shows the fraction of atoms with initial energy less than  $0.1 \text{ K} \times k_B$ ; this fraction has been multiplied by 2 so it

is roughly the same size as that of the final fraction. While the initial energy does depend on the orientation of the magnetic field axis, there is no direct correlation between how the initial low energy fraction and the final low energy fraction behave with angle. This shows that it is the effect of the orientation of the fields on how the atom decays and the final potential energy at that point which affects the final energy.

We performed calculations where the initial energy of the atoms was higher than that for the calculations presented here. We found that there was a larger effect when the energy was higher; for a case where the initial energy was approximately  $10\times$  higher than that presented here, we found that  $\max(P)/\min(P) \sim 4$ . Higher initial energy leads to a larger variation with orientation because higher energy atoms can move through a larger part of the trap volume which can lead to complex decay rates as a function of position like in figure 4(b).

## 5. Conclusions

We have presented a method for calculating the motion of a hydrogenic Rydberg atom in spatially varying electric and magnetic fields. The spatial dependence of the internal energy can be converted to a force and thus determines how the atom moves through a region with varying fields. This treatment should be accurate as long as the electric and magnetic fields are too weak to cause  $n$ -mixing of the levels. We also gave an approximation for how the atom decays into low principal quantum number; the treatment allows a simple calculation of the decay into all states of an  $n$ -manifold. In our treatment of the radiation, we assumed the atom decayed into a state with low- $n$  so that the subsequent cascade was fast. We did not treat the case where the atom decays through a sequence of small  $\Delta n$  transitions each of which is on a long time scale.

We used this basic formulation to investigate how Rydberg hydrogen atoms move and radiatively decay in a magnetic and electric field trap. We presented results on how the decay depends on the generalized angle  $\theta = \theta_1 + \theta_2$ . We chose a trap configuration that should be experimentally realizable and we chose reasonable initial conditions for the atoms. We presented results on how the decays occur versus time and the resulting energy distribution of atoms after the decay. We also showed that the orientation of the magnetic field could strongly affect the fraction of atoms at very low energies.

The authors of [9, 10] found that antihydrogen cooled during the radiative cascade when only the magnetic field was

present. The antihydrogen traps have substantial electric fields during the formation of the antihydrogen. Our results indicate that it might be unwise to ignore the interplay between electric and magnetic fields on the motion and decay of the Rydberg atoms. For the antihydrogen traps, some of the approximations in this paper will need to be revisited because many of the atoms start in high energy states where the effect from the electric and magnetic fields is too strong for perturbative methods.

## Acknowledgments

We thank F Merkt for discussion of this problem, for describing the current status of their experiment, and for providing us with data for their electric field. This work was supported by the National Science Foundation under grant no 0969530.

## References

- [1] Breeden T and Metcalf H 1981 *Phys. Rev. Lett.* **47** 1726
- [2] Townsend D, Goodgame A L, Procter S R, Mackenzie S R and Softley T P 2001 *J. Phys. B: At. Mol. Opt. Phys.* **34** 439
- [3] Yamakita Y, Procter S R, Goodgame A L, Softley T P and Merkt F 2004 *J. Chem. Phys.* **121** 1419
- [4] Vliegen E, Hogan S D, Schmutz H and Merkt F 2007 *Phys. Rev. A* **76** 023405
- [5] Hogan S D and Merkt F 2008 *Phys. Rev. Lett.* **100** 043001
- [6] Hogan S D, Seiler Ch and Merkt F 2009 *Phys. Rev. Lett.* **103** 123001
- [7] Andresen G B *et al* (ALPHA Collaboration) 2010 *Nature* **468** 673
- [8] Choi J-H, Guest J R, Povilus A P, Hansis E and Raithel G 2005 *Phys. Rev. Lett.* **95** 243001
- [9] Taylor C L, Zhang J and Robicheaux F 2006 *J. Phys. B: At. Mol. Opt. Phys.* **39** 4945
- [10] Pohl T, Sadeghpour H R, Nagata Y and Yamazaki Y 2006 *Phys. Rev. Lett.* **97** 213001
- [11] Lesanovsky I and Schmelcher P 2005 *Phys. Rev. Lett.* **95** 053001
- [12] Merkt F 2010 private communication
- [13] Merzbacher E 1998 *Quantum Mechanics* 3rd edn (New York: Wiley)
- [14] Pauli W 1926 *Z. Phys.* **36** 336
- [15] Penent F, Delande D, Biraben F and Gay J C 1984 *Opt. Commun.* **49** 184
- [16] Edmonds A R 1974 *Angular Momentum in Quantum Mechanics* (Princeton, NJ: Princeton University Press)
- [17] Seiler Ch, Hogan S D, Schmutz H, Agner J A and Merkt F 2011 *Phys. Rev. Lett.* **106** 073003
- [18] Press W H, Teukolsky S A, Vetterling W T and Flannery B P 1992 *Numerical Recipes* 2nd edn (New York: Cambridge University Press)